

IRMaGiC: Extending Luminous Red Galaxy Selection into the infrared with joint LSST and Roman HLIS Data

ZHIYUAN GUO,¹ C. W. WALTER,¹ ELI S. RYKOFF,^{2,3} AND THE LSST DARK ENERGY SCIENCE COLLABORATION

¹*Department of Physics, Duke University, Durham, NC 27708, USA*

²*SLAC National Accelerator Laboratory, Menlo Park, CA 94025, USA*

³*Kavli Institute for Particle Astrophysics and Cosmology, P.O. Box 2450, Stanford University, Stanford, CA 94305, USA*

ABSTRACT

We introduce IRMaGiC, an algorithm built based on RedMaGiC designed to enhance the selection of Luminous Red Galaxies (LRGs) across the redshift range $1 \leq z \leq 2$. We show that this method extends the capabilities of the redMaGiC algorithm by applying it to simulated photometric data from the Vera C. Rubin Observatory’s Legacy Survey of Space and Time (LSST) and the Nancy Grace Roman Space Telescope’s High Latitude Wide Area Survey (HLWAS). By integrating infrared band coverage from Roman HLWAS with LSST’s optical bands, IRMaGiC enables red-sequence calibration at higher redshifts. We demonstrate that IRMaGiC reduces scatter and bias in photometric redshift estimates for LRGs at higher redshift, providing more accurate redshift assessments compared to existing methods. Our findings suggest that incorporating infrared data can considerably improve the selection and redshift estimation of LRGs at higher redshift, offering substantial benefits for future cosmological surveys.

1. INTRODUCTION

Luminous red galaxies (LRGs) represent a fundamental component of the cosmic landscape, playing a pivotal role in the study of cosmological evolution and structure formation. These galaxies, characterized by their lack of significant star formation and their red colors due to older stellar populations, serve as important tracers of the mass assembly history of the universe (Choi et al. 2014; Khullar et al. 2022; Marsan et al. 2022; Zhuang et al. 2023; Beverage et al. 2024; Slob et al. 2024). Understanding the distribution and properties of LRGs across cosmic time provides insights into the mechanisms that drive galaxy evolution and the influence of environment on these processes. In cosmology, red, quiescent galaxies are often utilized as proxies to identify high-density environments like galaxy clusters and groups. The presence of the 4000Å break in their spectra makes them ideal candidates for accurate redshift estimation. Due to their brightness and distinct spectral features, these galaxies are easily detectable over a wide range of redshifts, making them ideal probes for studying the large-scale structure of the universe, with

such probes as Baryon Acoustic Oscillation (BAO) (Percival et al. 2007; Eifler et al. 2021; Carnero Rosell et al. 2022; DESI Collaboration et al. 2024) and Galaxy Clustering (GC) (Padmanabhan et al. 2007; Pandey et al. 2022; White et al. 2022; Sailer et al. 2024; Yuan et al. 2024).

There are various methods for selecting luminous red galaxies (LRGs) from a given survey. Surveys such as the Sloan Digital Sky Survey (SDSS) (Eisenstein et al. 2001) and the Dark Energy Spectroscopic Instrument (DESI) (Zhou et al. 2023a,b) use direct color cuts with different color combinations to identify LRG candidates across different redshifts. An alternative method is the red-sequence technique, which leverages the characteristic that predominantly red, luminous, and passively evolving red-sequence galaxies—known for their aged, metal-rich stellar populations—form a distinct ridge line (Visvanathan & Sandage 1977) at a specific redshift. This indicates that their colors vary minimally with magnitude in the color-magnitude diagram. By using a sample of red galaxies with known spectroscopic redshifts, one can calibrate and model the color-redshift evolution of the red sequence, known as the red-sequence template. This technique was initially developed for cluster-finding algorithms through the identification of LRGs using multi-band photometry. For example, the redMaPPer (Rykoff et al. 2014; Korytov et al. 2019)

Corresponding author: Zhiyuan Guo
 zhiyuan.guo@duke.edu

algorithm uses spectroscopic samples from SDSS to iteratively fit a red-sequence template to identify clusters in SDSS and the Dark Energy Survey (DES) (Dark Energy Survey Collaboration et al. 2016). Similarly, the CAMIRA (Oguri 2014; Oguri et al. 2017a) algorithm employs stellar population synthesis models, also calibrated using SDSS data, to predict the colors of red-sequence galaxies and identify clusters in the Subaru Hyper Suprime-Cam survey (HSC) (Aihara et al. 2018).

Further advancements have built upon the calibrated red-sequence template to create an effective red galaxy selection algorithm based solely on photometric data, enabling the selection of LRGs in galaxy samples while simultaneously providing accurate photometric redshift estimates. For example, the RedMaGiC algorithm (Rozo et al. 2016) builds upon the calibrated red-sequence template from RedMaPPer to select and generate LRG catalogs for SDSS and DES. As mentioned earlier, in this algorithm the red sequence is initially calibrated using cluster-finding algorithms because red galaxies typically reside at the centers of clusters, and neighboring galaxies within the same cluster are likely to share the same redshift as the central red galaxy. This method thus leverages the red central galaxies to extend the red-sequence calibration to fainter magnitudes, thereby increasing the number of data points available for the calibration process. However, with enough spectroscopic galaxy samples, the red-sequence template can be also calibrated independently without relying on galaxy clusters. For example, Vakili et al. (2019) calibrated a red-sequence template for the Kilo-Degree Survey (KiDS) (de Jong et al. 2013) Data Release 3 (de Jong et al. 2017) using ugr photometry and spectroscopic galaxies from the overlapping regions of GAMA (Driver et al. 2011) and SDSS. In follow-up work, Vakili et al. (2023) extended this calibration using KiDS DR4, incorporating The VISTA Kilo-degree Infrared Galaxy (VIKING) Survey (Edge et al. 2013) ZYJHKs near-infrared bands. This calibrated template was then used to generate RedMaGiC-like galaxy samples from KiDS with similar photometric redshift performance. However, previous surveys have been limited to probing LRGs up to redshift $z < 1$ due to the constraints of optical band coverage, as the 4000Å break shifts into infrared wavelength at higher redshifts.

In this paper, we introduce **IRMaGiC**, the InfraRed extension of RedMaGiC, and apply it to simulated datasets from two Stage IV dark energy surveys as categorized by the Dark Energy Task Force (Albrecht et al. 2006): the Vera C. Rubin Observatory’s Legacy Survey of Space and Time (Ivezić et al. 2019) (hereafter referred to as LSST) and the Nancy Grace Roman Space Tele-

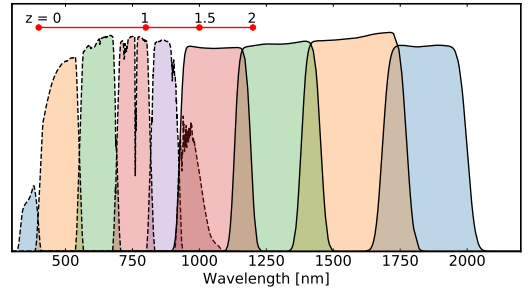


Figure 1. Throughput curves for the six LSST filters and four Roman filters. From left to right, the LSST u, g, r, i, z, y filters are represented by black dashed lines, while the Roman F106, F129, F158, F184 filters are shown with black solid lines. The red solid horizontal line marks the wavelength of the 4000Åbreak as the galaxy spectra get redshifted. This illustration is intended to demonstrate the overall shape and wavelength coverage of the filters and does not represent the actual throughput values.

scope’s High Latitude Wide Area Survey (Spergel et al. 2015; Akeson et al. 2019) (hereafter referred to as *Roman* HLWAS). Our goal is to adapt a RedMaGiC-like algorithm for selecting Luminous Red Galaxy (LRG) samples within the redshift range of $1 \leq z \leq 2$. This is made feasible because *Roman* HLWAS includes infrared wavelength coverage, complementing the optical bands of LSST as shown in Figure 1. Thus, it becomes possible to extend the red-sequence template to higher redshifts. Our approach is similar to that of Vakili et al. (2019) and Vakili et al. (2023), as we rely on a sufficient supply of spectroscopically confirmed red galaxies from the spectroscopy component of the *Roman* HLWAS, the High Latitude Spectroscopic Survey (hereafter HLSS), for red-sequence template calibration.

This paper is organized as follows: In Section 2, we describe the simulated datasets used in this study for LSST, Roman HLIS, and Roman HLSS. Section 3 provides an overview of the IRMaGiC algorithm, including red-sequence calibration (Section 3.5), the implementation of the Roman HLSS red galaxy efficiency curve (Section 3.3), and the candidate selection process (Section 3.6). We also introduce a novel method of identifying high-redshift ($z > 1$) red galaxy candidates for red-sequence calibration in Section 3.2. In Section 4, we evaluate the photometric redshift performance of our LRG samples and compare with those obtained from existing photometric redshift estimation codes. We also compare our LRG samples with existing LRG samples at lower redshifts, specifically the cosmoDC2/DC2 Red-

MaGiC catalogs¹ in Section 4. Additionally, we investigate how different assumptions about the area of overlap regions between LSST and *Roman* HLIS affect the maximum achievable redshift range with our red-sequence template. Finally, we summary our findings in Section 5.

2. DATA

2.1. LSST DC2

The LSST is a ground-based photometric survey designed to observe approximately $20,000 \text{ deg}^2$ of the sky during its 10-year mission across *ugrizy* bands (LSST Science Collaboration et al. 2009). The survey consists of two main components: the Wide-Fast-Deep (WFD) survey, covering $18,000 \text{ deg}^2$, and the Deep Drilling Fields (DDFs). This study focuses on the WFD, which is particularly suited for dark energy probes such as weak lensing, galaxy clustering, and Type Ia supernovae (The LSST Dark Energy Science Collaboration et al. 2018). Given the unprecedented scale of data production by LSST, there is a crucial need to develop and verify software pipelines for analyzing the released data. To address this, the LSST Dark Energy Science Collaboration (DESC) has initiated a series of data challenges aimed at developing an end-to-end simulation pipeline to generate LSST-like data products (LSST Dark Energy Science Collaboration 2012). The LSST simulation used in this study is based on the second data challenge (DC2) (LSST Dark Energy Science Collaboration (LSST DESC) et al. 2021). The simulated DC2 sky survey replicates LSST observations over six optical bands *ugrizy* within a WFD area of approximately 300 deg^2 and a DDF area of 1 deg^2 , reflecting the expected depth over five years of the planned 10-year survey.

The DC2 simulation starts with the large-volume N-body cosmological simulation, Outer Rim (Heitmann et al. 2019) to generate a realistic extragalactic catalog, cosmodc2 (Korytov et al. 2019), which includes galaxy properties such as shapes, redshifts, and magnitudes. Instance catalogs for specific telescope pointings are then used to create synthetic images using the DESC image simulation package IMSIM², which simulates telescope and atmospheric effects. These images are subsequently processed through the LSST Science Pipelines to produce data products analogous to those expected from the actual LSST survey. For additional information, we direct the readers to LSST Dark En-

ergy Science Collaboration (LSST DESC) et al. (2021); LSST Dark Energy Science Collaboration et al. (2021).

In this study, we use the static object catalog, `dc2_object_run2.2i_dr6a_with_photoz`, which processes data up to year 5 (DR5) of LSST and provides necessary information such as measured photometry, detected position (RA,DEC) and object types. The catalog is accessed via the `GCRcatalog` interface³. We use the measured composite model (cModel) photometry as recorded in the catalog for galaxy magnitudes and corresponding errors. The galaxy/star separation is done by filtering the catalog via the `extendness` parameter ranging from 0 to 1, which indicates whether the light from an object is concentrated (point-like) or spread out (extended). In this study, we select objects with `extendness > 0.5` as galaxy candidates from LSST DC2.

2.2. Roman simulation

The Roman High Latitude Survey consists of two components: an imaging component, the High Latitude Imaging Survey (HLIS), and a spectroscopy component, the High Latitude Spectroscopy Survey (HLSS). Based on the current *Roman* reference survey (Troxel et al. 2023; Wang et al. 2022), the HLIS and HLSS will observe a 2000 deg^2 region of the sky, fully within the LSST footprint, over a five-year period in four near-infrared bands: F106, F129, F158, and F184, enabling joint analyses between the two surveys. In this paper, we denote these four *Roman* bands as Y, J, H, F.

The Roman galaxy sample used in this study is derived from the joint Roman HLIS-LSST image simulation presented in Troxel et al. (2023). This simulation is based on the updated Roman HLIS image simulation pipeline, which includes a realistic Point Spread Function (PSF), sensor physical effects, and chromatic rendering (Troxel et al. 2023). The simulation focuses on a 20 deg^2 region of the LSST-DC2 universe, spanning $51^\circ < \text{RA} < 56^\circ$ and $-42^\circ < \text{DEC} < -38^\circ$, for the five-year depth of the HLIS. This joint simulation provides an excellent testbed for joint survey analysis. It uses the same basic truth input as the DC2 simulation, with adjustments specifically tailored for the need of Roman HLIS. For further details, the readers are referred to Troxel et al. (2023).

Object detection and measurements are performed on coadded images in each HLIS band using SourceExtractor (Bertin & Arnouts 1996). In this study, we use the provided `mag_auto` values for galaxy magnitudes and

¹ <https://github.com/LSSTDESC/gcr-catalogs>

² <https://github.com/LSSTDESC/imSim>

³ <https://github.com/LSSTDESC/gcr-catalogs>

their associated errors in each Roman band. For the Roman simulated data, we rely on the truth information to select galaxies. We cross-reference the detection catalog generated by SourceExtractor with the input truth galaxy catalog by matching objects based on their celestial coordinates, which is further refined by selecting those with the closest photometry. It is important to note that the Roman science pipeline has not yet been finalized, so there may be discrepancies between the results presented here and those from future analyses, and we defer the star/galaxy separation for the Roman HLIS to a future study.

2.3. Cross matching

A combined galaxy sample from both surveys is essential to calibrate a red-sequence model for the targeted redshift range ($1 < z < 2$). Objects that show significant detections in the optical bands may not necessarily have strong detections in the near-infrared bands, and vice versa. Therefore, crossmatching the galaxy catalogs from the two surveys is crucial to ensure that the galaxies in the combined catalog have significant detections in both. This crossmatching is performed based on positional (RA, DEC) alignment, retaining matches within 0.2 arcseconds and requiring significant detections ($> 5\sigma$) in the Rubin LSST i, z, and Roman Y, J, H, and F bands. This is accomplished by setting the following parameter thresholds on the DC2 catalog: `snr_i_cModel` ≥ 5 and `snr_z_cModel` ≥ 5 , and by ensuring `flux_auto/flux_auto_err` ≥ 5 in the Roman catalog. In this study, we focus primarily on relatively bright galaxies. To verify the positional matching results, we cross-checked with information from the truth catalogs of the DC2 and Roman simulations. We find that for galaxies with $m_H > 23$, 99% have truth matches based on galaxy id, confirming that the cross-matched sources from both catalogs represent the same galaxies.

2.4. Roman Grism spectroscopy

As previously noted, a sample of spectroscopically confirmed red galaxies in the NIR/IR spectrum is essential for precise calibration of the red-sequence template at higher redshift. In this study, we assume that the spectroscopic galaxy sample will be sourced from *Roman* HLSS. The *Roman* grism enables spectroscopy at a resolution of $R = 460\lambda/\mu\text{m}$ for wavelengths in the range $\lambda = 1 - 1.93\mu\text{m}$. In [Guo et al. \(2024\)](#), we conducted a detailed analysis of the Roman grism's capability to measure spectroscopic redshifts (spec-z) for red, quiescent galaxies via simulation. Then we predicted the expected redshift recovery rate for these galaxies observed in the Roman HLSS. Further details are discussed in Section 3.3.

3. METHOD

3.1. Algorithm overview

Red-sequence galaxies display a consistent color-redshift relationship, aligning along a defined ridge in the color-magnitude diagram within a certain intrinsic scatter at any given redshift. This feature can be characterized empirically by the following red-sequence template (hereafter RS-template), which is modeled through a set of the parameters smoothly evolving as a function of redshift:

$$\langle \mathbf{c}|z, m \rangle = \mathbf{a}(z) + \mathbf{s}(z)[m - m_{\text{ref}}(z)] \quad (1)$$

where z is the redshift, \mathbf{c} is the color vector i - z, z - Y, Y - J, J - H, H - F of a galaxy, $\mathbf{a}(z)$ and $\mathbf{s}(z)$ are the redshift-dependent intercept (mean color) and slope of the ridge-line. m is the reference magnitude in the reference band. According to [Rozo et al. \(2016\)](#), the reference band should lie redwards of the 4000Å break. In this study, We choose F as the reference band. $m_{\text{ref}}(z)$ is defined as the pivot point of the color-magnitude relation and it can be chosen arbitrarily. In this study, we follow [Rozo et al. \(2016\)](#) and set it as the median magnitude of the seed galaxies in the reference band. Additionally, a color covariance matrix, \mathbf{C}_{tot} is defined for every galaxy.

$$\mathbf{C}_{\text{tot}} = \mathbf{C}_{\text{obs}} + \mathbf{C}_{\text{int}}(z) \quad (2)$$

It is composed of two component \mathbf{C}_{obs} , the observed color covariance, for any color pair with $C_i = m_a - m_b$ and $C_j = m_q - m_p$,

$$\mathbf{C}_{\text{obs}}(z) = \begin{pmatrix} \sigma_a^2 + \sigma_b^2 & \gamma \\ \gamma & \sigma_q^2 + \sigma_p^2 \end{pmatrix} \quad (3)$$

with

$$\gamma = \begin{cases} -\sigma_q^2 & \text{if } b = q \\ 0 & \text{if } b \neq q \end{cases} \quad (4)$$

and $\mathbf{C}_{\text{int}}(z)$, the intrinsic red-sequence color covariance. The calibration of the red-sequence parameters $\mathbf{a}(z)$, $\mathbf{s}(z)$ and $\mathbf{C}_{\text{int}}(z)$ is discussed in detail in Section 3.5.

The goal is to estimate the photometric redshift of a galaxy with a certain magnitude m and color vector \mathbf{c} with a calibrated RS-template. The redshift probability of a red galaxy with H band magnitude m , and color vector \mathbf{c} can be calculated as:

$$\begin{aligned} P(z|\mathbf{c}, m) &= \frac{P(\mathbf{c}, m, z)}{P(\mathbf{c}, m)} \\ &\propto P(\mathbf{c}|m, z)P(m|z)P(z) \end{aligned}$$

We are interested in calculating the likelihood

$$\mathcal{L} = P(\mathbf{c}|m, z)P(m|z)P(z) \quad (5)$$

The first term $P(\mathbf{c}|m, z)$ is defined as:

$$P(\mathbf{c}|m, z) \propto \exp \left[-\frac{1}{2} \chi_{\text{red}}^2(z) \right] \quad (6)$$

where

$$\chi_{\text{red}}^2(z) = (\mathbf{c} - \langle \mathbf{c}|z, m \rangle)^T \mathbf{C}_{\text{tot}}^{-1} (\mathbf{c} - \langle \mathbf{c}|z, m \rangle) \quad (7)$$

and \mathbf{C}_{tot} is the galaxy color variance defined above in Equation 2. The second term $P(m|z)$ serves as a redshift-dependent luminosity filter and is modeled assuming the galaxies follow a Schechter luminosity function:

$$P(m|z) \propto 10^{-0.4(m - m_*(z))(\alpha+1)} \exp \left[-10^{-0.4(m_i - m_*(z))} \right]$$

Following Rozo et al. (2016), the parameter α is set to 1. $m_*(z)$ is the characteristic magnitude in the reference band. And it is computed using the Bruzual & Charlot stellar population synthesis code (Bruzual & Charlot 2003) implemented in the EzGal Python package⁴ assuming a solar metallicity, a Salpeter initial mass function (Salpeter 1955), and a single star formation burst at $z = 3$ following Rozo et al. (2016). The normalization condition is computed from the BC03 model using the Roman F bandpass. Finally, the last term, $P(z)$, the redshift prior, is defined as the derivative of the comoving volume with respect to redshift.

$$p(z) \propto \frac{dV}{dz} = (1+z)^2 D_A^2(z) c H^{-1}(z) \quad (8)$$

where c is the speed of light, $H(z)$, $D_A(z)$ are the Hubble parameter and the angular diameter distance as a function of redshift. It is important to note that this prior is implemented solely for the purpose of redshift fitting in the likelihood function. We do not apply a constant comoving density constraint to the final Red-MaGiC sample, as will be discussed in Section 3.6. Thus, the final expression for the redshift likelihood function is expressed as:

$$\begin{aligned} \ln \mathcal{L}(z) = & -\frac{1}{2} \chi_{\text{red}}^2(z) - \frac{1}{2} \ln \det(\mathbf{C}_{\text{tot}}(z)) \\ & + \ln P(m|z) + \ln \left| \frac{dV}{dz} \right| \end{aligned} \quad (9)$$

The photometric redshift $\widetilde{z}_{\text{red}}$ is computed as the integral of the likelihood function over the redshift range:

$$\langle \widetilde{z}_{\text{red}} \rangle = \frac{\int dz \mathcal{L}(z) z}{\int dz \mathcal{L}(z)} \quad (10)$$

The tilde is used to indicate that this value is an initial estimate of IRMaGiC photo-z, which is further refined using an afterburner (see Section 3.7). The corresponding photometric redshift error σ_z is computed as:

$$\sigma_z^2 = \langle z^2 \rangle - \langle z \rangle^2 \quad (11)$$

Additionally, for each galaxy, we assigned a χ_{red}^2 value, corresponding to the chi-square value at the redshift that maximizes the log-likelihood function in Equation 9, and a luminosity ratio,

$$l(m, \widetilde{z}_{\text{red}}) = \frac{L}{L_*} = 10^{-0.4(m - m_*(\widetilde{z}_{\text{red}}))} \quad (12)$$

where m_* and L_* are the characteristic magnitude and luminosity as discussed above.

χ_{red}^2 indicates how well a galaxy's photometry is fitted by the calibrated red-sequence template (See Section 3.5), while luminosity ratio is used to determine whether a galaxy satisfy the luminosity threshold (See Section 3.6). The two quantities are estimated for all detected galaxies within the simulation region and are later used for LRG candidate selection (See Section 3.6).

3.2. Seed galaxy selection

A set of LRGs with accurate spectroscopic redshift (spec-z) is essential for calibrating the red sequence. This set of galaxies is known as the seed galaxy sample. Previous studies have selected LRGs using color cuts (Eisenstein et al. 2001; Oguri et al. 2017b; Crocce et al. 2019; Zhou et al. 2023c) or by applying a Gaussian mixture model (Rykoff et al. 2016; Vakili et al. 2019) within narrow redshift bins ($\Delta z \approx 0.02$), leveraging the color bimodality of the two populations to differentiate between red and blue galaxies. However, these methods are primarily effective for galaxies at low redshifts ($z < 1$) and are not suitable for this study for two main reasons. First, the distinction between blue and red galaxies diminishes at higher redshifts, rendering a direct cut in color space ineffective. Second, although the Roman HLSS will provide spectroscopic redshifts for galaxies, the efficiency curve of LRGs significantly diminishes for fainter cases. This efficiency decline implies that when galaxies with spectroscopic redshifts are segmented into narrow bins, the distribution will be predominately composed of blue populations. Consequently, it becomes challenging to assemble a sufficiently

⁴ <https://github.com/cmancone/easyGalaxy>

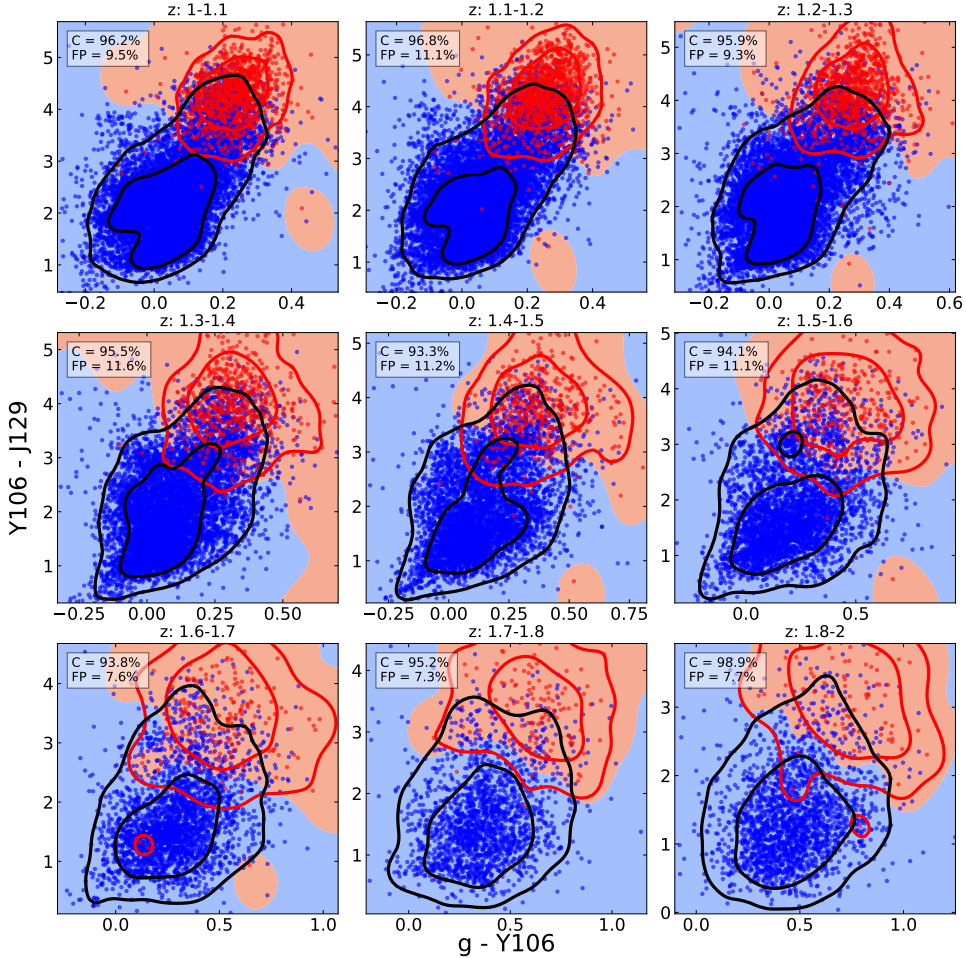


Figure 2. The observed (Y - J) versus (g - Y) colors. Data are shown at different redshift bins, from $z = 1$ to $z = 2$. Galaxies are color coded depending on their sSFR and Red-sequence flag based on truth information. The red dots are quiescent galaxies and blue dots are star-forming galaxies. The black and red solid lines show the 68 and 95 percent contours of the number density of star-forming and quiescent, red galaxies respectively. The red and blue contours show the classification boundary from SVM. On the top left-hand side of each panel, we report the completeness (C) and False-positive (FP) fraction of the red, quiescent galaxy selection.

large sample of red galaxies within these narrow bins to enable a meaningful Gaussian mixture model that can effectively characterize their distribution.

The Euclid Space Telescope (hereafter Euclid)⁵ is another deep-space imaging survey operating at optical and near-infrared wavelengths, featuring broad-band filters, Y_E, J_E, H_E , similar to Roman. We use the subscript 'E' to differentiate these from the Roman bands.

For Euclid, Bisigello et al. (2020) have developed a color-color cut criteria to separate quiescent galaxies from star-forming galaxies up to $z = 2.5$ using color combinations such as, $VIS-Y_E, J_E-H_E$ and $u-VIS, VIS-J_E$, where 'VIS' refers to the Euclid Visible Instrument, and 'u' represents the u-band from the Canada-France Imaging Survey (CFIS), which serves as the complementary ground-based survey for Euclid in the north. In this study, we adopt a similar strategy, combining the near-infrared filters from Roman with the optical bands from LSST to select seed red-sequence galaxies. We leverage

⁵ <http://sci.esa.int/euclid/>

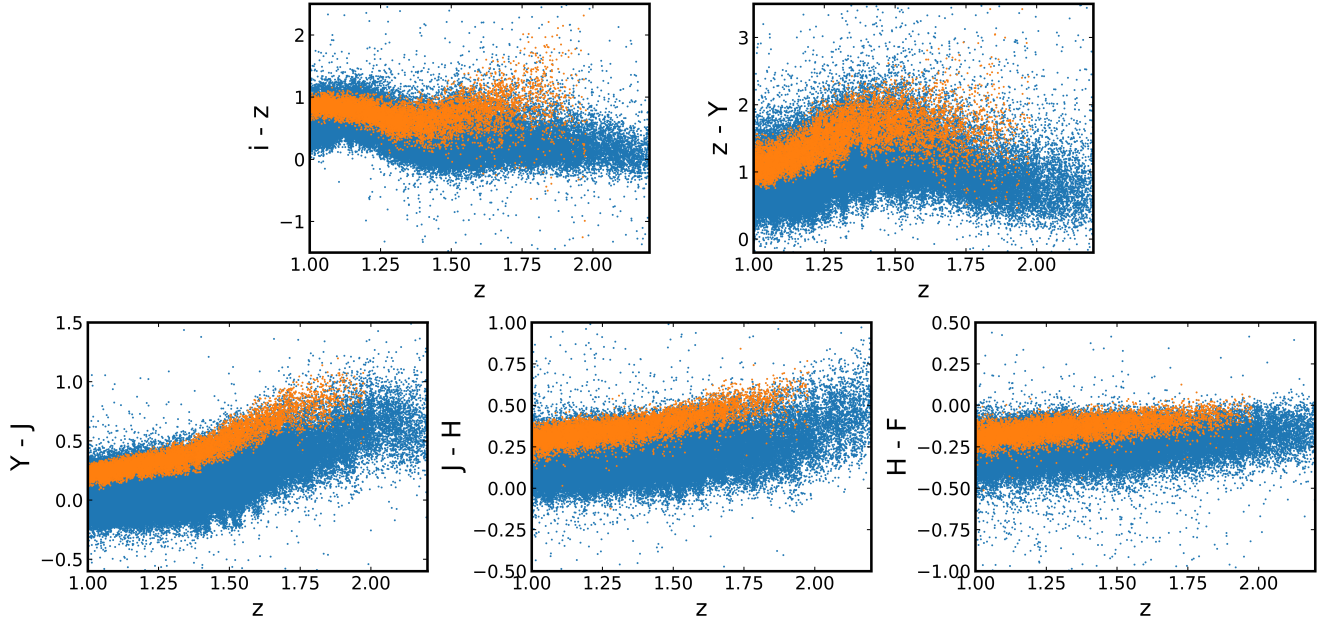


Figure 3. Color evolution versus true redshift for all galaxies with $m_H \leq 22$ mag cross-matched from the 20 deg^2 region of the Roman simulation and LSST DC2. The blue points represent all galaxies included in this study, while the orange points indicate the seed galaxies selected for calibrating the red-sequence template. The five panels illustrate the redshift dependence of the $i - z$, $z - Y$, $Y - J$, $J - H$, and $H - F$ colors. Here, the i and z band magnitudes are sourced from LSST-DC2 measurements, whereas the Y , J , H , and F magnitudes are derived from the Roman simulation.

truth information from simulated data, such as star formation rates and red-sequence flags, to label red and blue galaxy populations. These labels, along with the corresponding photometric measurements, are used to train decision boundaries, which can then be applied to future real data where ground-truth information is not available.

The first step is to distinguish between quiescent and star-forming galaxies. Given that the efficiency curve of the Roman grism for red galaxies approaches zero at $m_H = 22$ (Guo et al. 2024), we apply a magnitude cut on the joint galaxy sample, focusing only on galaxies with $m_H \leq 22$. This magnitude cut discards fainter galaxies, facilitating a clearer identification of separations between the two populations. In literature, many works (Paspaliaris et al. 2023; Florez et al. 2020; Stefanon et al. 2013; Fontanot et al. 2009) separated quiescent galaxies from star-forming populations based on a fixed threshold in specific star formation rate (sSFR), calculated as follows:

$$\text{sSFR} = \frac{\text{SFR}}{M_{\text{star}}} \quad (13)$$

where SFR is the stellar formation rate and M_{star} is the stellar mass. Following those studies, we adopt an sSFR threshold of quiescent galaxies:

$$\log_{10}(\text{sSFR}/\text{yr}^{-1}) \leq -11 \quad (14)$$

while star-forming galaxies have

$$\log_{10}(\text{sSFR}/\text{yr}^{-1}) > -11 \quad (15)$$

Here we use the quantities `totalStarFormationRate` and `stellar_mass` provided in the DC2 catalog to calculate an sSFR for every galaxy. Moreover, the DC2 truth catalog provides a 'red-sequence' flag for each galaxy. We further refine our sample of quiescent galaxies by selecting those with the `is_on_red_sequence` flag set to True, ensuring a purer sample of red, passively evolved galaxies. We then bin quiescent and star-forming galaxies into redshift bins to explore the effectiveness of various color combinations available from LSST and Roman in distinguishing quiescent galaxies from the star-forming population in each redshift bin. It is important to note that this binning assumes the availability of only photometric redshifts (photo-z) from LSST for all galaxies. This assumption is made because, in reality, spectroscopic redshifts (spec-z) will not be available for all observed red galaxies, resulting in an insufficient number of red galaxy samples to establish a clear separation between the two populations. Therefore, we propose a strategy where we initially utilize photometric data from both surveys and use photo-z from LSST to galaxies in wide redshift bins $\Delta_z = 0.1$ to select red galaxy candidates, then subsequently using candidates with spec-z from the *Roman* HLSS as the seed

galaxies to calibrate the red-sequence template. According to the LSST official documents⁶, the minimum performance targets for photo-z should result in a standard deviation of $z_{\text{true}} - z_{\text{photo}}$ of $\sigma_z \leq 0.05(1 + z_{\text{photo}})$. We thus compute mock photo-z based on the true redshift using:

$$z_{\text{photo}} = z_{\text{true}} + \epsilon \quad (16)$$

where $\epsilon \sim N(0, \sigma^2)$ and $\sigma = 0.05(1 + z_{\text{true}})$.

We find that the color combination of (g - Y) and (Y - J) offers the most robust separation between the two populations. The nine panels in Figure 2 show the (g - Y) versus (Y - J) distribution of star-forming and quiescent galaxies in each redshift bin. The black and red solid lines in each panel show the 68 and 95 percent contours of the number density of the two populations. It is important to note that due to the scarcity of red galaxies beyond $z = 1.8$, we use a wider bin of $\Delta_z = 0.2$ for the final bin, compared to $\Delta_z = 0.1$ used for the earlier bins. The well-separated 68% contours indicate the presence of the two galaxy populations in this color-color space. However, the 95% contours reveal some overlaps, suggesting that quiescent galaxies remain partially contaminated by the star-forming population.

Comparing to the approach of Bisigello et al. (2020), who implement a linear boundary in the color-color space to separate the two populations, we have adopted a more robust nonlinear approach. This is achieved using Support Vector Machine (SVM) with a radial basis function (**rbf**) kernel to estimate a nonlinear decision boundary in the 2D color-color space. The SVM model includes two hyper-parameters: **C**, the regularization parameter, and **gamma**, the kernel coefficient. We optimized these parameters by exploring the best combination on a parameter grid of $C \in [0.01, 0.1, 1, 10]$ and $\gamma \in [0.1, 1]$ with a step size of 0.1. Optimization was conducted using the GridSearchCV function in **scikit-learn** (Pedregosa et al. 2011), employing a custom scoring function defined as $C(1 - \text{FP})$ following Bisigello et al. (2020). Here, **C** represents the completeness, defined as the fraction of true quiescent and red galaxies correctly classified within the decision boundary, while **FP** denotes the false-positive fraction, representing the proportion of star-forming, blue galaxies incorrectly classified within the boundary. We constrained the range of γ to smaller values in purpose to prevent over-fitting. The final decision boundaries are delineated by blue and red regions in Figure 2. Additionally, the completeness and false-positive fraction, given the boundary, are displayed within each panel. It is evident

that this approach allows us to achieve an high completeness of approximately 95% with relatively low FP fraction ($\approx 10\%$).

However, it is important to note that the effectiveness of this method may vary across different galaxy samples, as we have implemented a stringent magnitude cut in our analysis based on the anticipated performance of the Roman grism for measuring spectroscopic redshifts of red galaxies. Additionally, variations in the photometry measurements could influence the decision boundary. Therefore, it is necessary to retrain the SVM boundaries before applying them to the real data as simulated data being measured from updated pipelines become available from both the Roman and LSST surveys in the future. In this study, we select seed galaxies based on the SVM boundaries in Figure 2. Figure 3 shows color versus true redshift (spec-z) distribution for the galaxy sample used in this study after making the magnitude cut. The orange points highlight the final seed galaxies selected for the red-sequence template calibration.

3.3. Roman Grism red galaxy efficiency curve

In this study, we have assumed that spectroscopic redshift of all the seed galaxies will be sourced from the *Roman* high latitude spectroscopy survey (HLSS). And we use the truth redshift recorded in the truth catalog as the spectroscopic redshift. However, not all galaxies selected based on the method outlined in Section 3.2 will have reliable spectroscopic counterparts from the *Roman* HLSS. Thus, it is important to account for the realistic performance of the *Roman* HLSS in estimating spec-z for LRGs. Given the absence of previous studies focused on assessing this aspect, we have developed a *Roman* grism image simulation to extract and analyze this necessary information.

We provide a brief summary here and direct readers to Guo et al. (2024) for more comprehensive details. Using simulated direct images from Troxel et al. (2023) as the reference, we simulate *Roman* grism images based on the *Roman* grism's instrumental properties, expected background levels, and the *Roman* reference survey design. Following this, we extract spectra of red, quiescent galaxies from the simulated grism images and perform redshift fitting. The simulation and proceeding analysis are all done by using the Grism Redshift and Line Analysis software, **Grizli**⁷ (Brammer 2019). Our analysis is focused on evaluating the redshift recovery efficiency, defined as the fraction of red, quiescent galaxies with high-confidence spectroscopic redshift estimates with respect

⁶ <https://dmtn-049.lsst.io/DMTN-049.pdf>

⁷ <https://github.com/gbrammer/grizli>

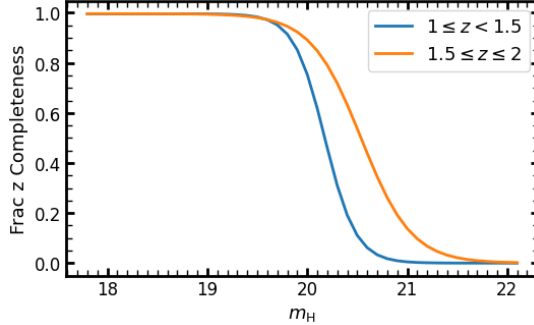


Figure 4. Roman grism efficiency curve for red, quiescent galaxies derived in Guo et al. (2024).

to the total population of red galaxies in the simulation, across a redshift range of 1 to 2.

The final data product is the red galaxy efficiency curve, which reflects the fraction of red galaxies with high signal-to-noise ratio ($\text{SNR} > 5$) and have reliable spec-z measurements ($(z_{\text{spec}} - z_{\text{truth}})/(1+z_{\text{truth}}) \leq 0.01$), as a function of H band magnitude. This curve, derived based on the *Roman* reference survey strategy, acts as a selection function indicating the probability of a red galaxy at a specific redshift and with a specific magnitude being identified and having redshift measured accurately. Additionally, we observed that, with similar brightness, red galaxies at higher redshifts ($z \geq 1.5$) typically exhibit more accurate redshift fitting results compared to those at lower redshifts. This improved accuracy is attributed to the Roman grism's wavelength coverage of $1\mu\text{m} - 2\mu\text{m}$, which aligns with the redshifted 4000\AA break in galaxies within the redshift range of $1.5 \leq z \leq 4$. The presence of the break in the extracted spectra enhances the precision of redshift measurements. Thus, we apply two sets of efficiency curves, as shown in Figure 4, to select seed galaxy in two redshift intervals, $1 \leq z \leq 1.5$ and $1.5 \leq z \leq 2$ respectively from the seed galaxy sample.

3.4. Scaling of overlap region

One major issue we identified after incorporating the red galaxy efficiency curve into the seed galaxy selection pipeline is that there are not enough seed galaxies at higher redshift that can be used for calibration. This is because higher-redshift galaxies tend to be fainter and the efficiency curve drops significantly at fainter magnitudes. However, the simulation we work with only covers a 20 deg^2 overlapping field of *Roman* and LSST, and the current *Roman* reference survey assumes a full overlap region of 2000 deg^2 . To fully utilize the overlap, we assume that the current simulated 20 deg^2 field is representative of the entire survey area. We then repeatedly apply the efficiency curve to the initial seed galaxy sample

as the assumption of the coverage of the overlapping region increases. For example, when considering a 40 deg^2 region, the selection function is applied twice, and the samples from both runs are combined to form the final seed galaxy sample. This inevitably introduces duplicate galaxies—particularly when extended to larger regions—resulting in a sample increasingly dominated by duplicates, especially at lower redshifts ($1 < z < 1.5$), where most bright galaxies reside and the efficiency curve approaches unity for such galaxies. This may lead to over-simplified results. However, this approach still provides valuable insights into how improved statistics from a larger overlap region can allow us to identify LRGs and measure redshift at higher redshifts. The results presented in the following sub-sections are based on a full overlap of 2000 deg^2 for illustrative purposes. We will discuss results based on different assumptions regarding the overlap area in Section 4.4.

3.5. Red-sequence template calibration

The red-sequence template is defined by four parameters: intercept $\mathbf{a}(z)$, slope, $\mathbf{s}(z)$, intrinsic scatter, $\mathbf{C}_{\text{int}}(z)$, and reference magnitude, $m_{\text{ref}}(z)$ in Eq 1. This section outlines the calibration process for these parameters by using the seed galaxy samples described in previous sections, which closely follows the methodology presented in Rykoff et al. (2014).

Step 1: Pivot magnitude estimations: The first step of calibration is to estimate pivot magnitudes $m_{\text{ref}}(z)$, which is estimated using cubic spline interpolation based on a set of $m_{\text{ref}}(z_i)$ values. These are calculated as the median magnitude of the seed galaxies at spline nodes i , which are uniformly distributed from $z = 1$ to $z = 2$.

Step 2: Perform initial estimates of mean-color redshift relation and its width to refine seed galaxy sample: Having defined the pivot magnitudes as function of redshift, The second step is to perform an initial estimate of the mean color-redshift relation, $\tilde{c}(z)$ for each color. This is achieved by minimizing the objective function:

$$O = \sum_i |c_i - \tilde{c}(z_i)| \quad (17)$$

where i sums over all seed galaxies used for calibration, and $\tilde{c}(z)$ is determined through spline interpolation, with the spline node values—minimized in Eq 17—defined on a redshift grid spaced at intervals of 0.1. The minimization is performed by using the `scipy.optimize.minimize` function with the 'L-BFGS-B' method. Next the initial estimation of mean-color is used to calculate an initial estimation of width of the color-redshift relation for each color, $\tilde{\sigma}_{\text{int}}(z)$. This is done by minimizing the objective func-

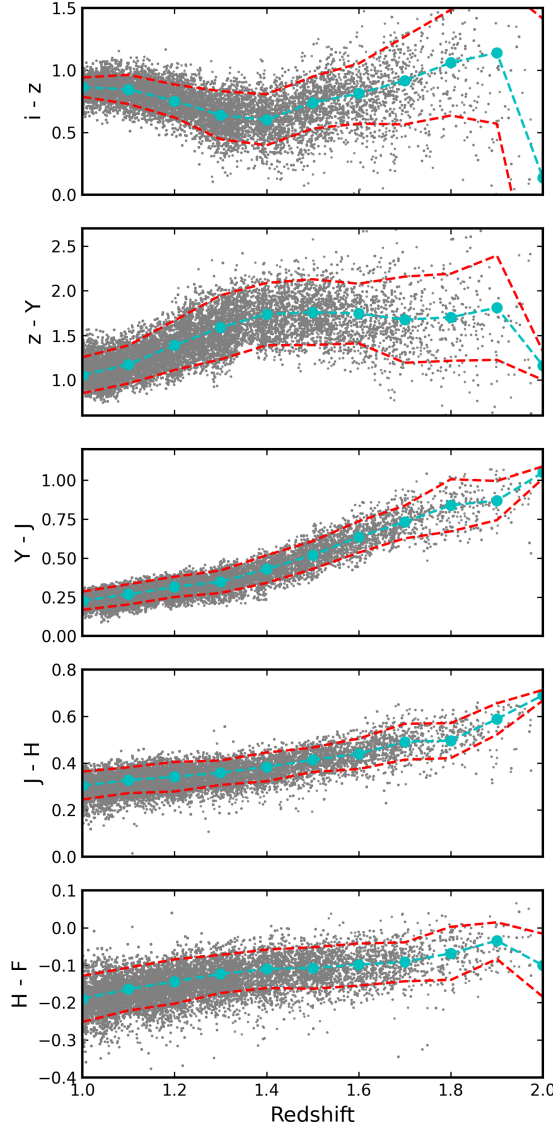


Figure 5. Color ($i - z$, $z - Y$, $Y - J$, $J - H$, $H - F$) as a function of redshift for the selected seed galaxies. The cyan points indicate the $a(z)$ values at the spline node positions, and the cyan, dashed lines are the spline interpolation. The red, dashed lines indicates the $3\sigma_{\text{int}}$ range. Conversely, the larger number of outliers in the five colors above reflects the fact that the photometric errors are larger than the intrinsic width of the red sequence.

tion,

$$O = \sum_i |c_i - \tilde{c}(z_i) - \text{MAD}| \quad (18)$$

where MAD stands for the median absolute deviation about the median and it is related to $\tilde{\sigma}_{\text{int}}(z)$ by:

$$\tilde{\sigma}_{\text{int}}(z) = 1.4826 \times \text{MAD} \quad (19)$$

Next, we refine the seed sample by selecting galaxies within $\tilde{\sigma}_{\text{int}}(z)$ of the median color. This selection cri-

terion ensures that the calibration leverages the core of the red galaxy distribution, minimizing potential bias from bluer galaxies.

Step 3: Calibration of intercept, slope and intrinsic scatter: The updated seed galaxy sample and pivot defined, we now turn to calibrate the intercept, $\mathbf{a}(z)$, slope $\mathbf{s}(z)$ and intrinsic scatter σ_{int} of the red-sequence relation in Eq 1. Similarly, cubic spline interpolation functions are used to parameterize smoothly evolving functions of redshift. In this study, we choose 0.05, 0.1 and 0.1 as the node spacing for intercept, slope and intrinsic scatter respectively. This is achieved by minimizing the negative log-likelihood function for each color respectively:

$$O = - \sum_i \tilde{\mathcal{L}}_i \quad (20)$$

$$= - \sum_i \log \left[\frac{1}{\sqrt{2\pi\sigma_{\text{tot}}^2}} \exp \left(-\frac{1}{2} \left(\frac{c_i - c(z, m)}{\sigma_{\text{tot}}} \right)^2 \right) \right] \quad (21)$$

where $c(z, m)$ is given by Eq 1, c_i is the color for each seed galaxy, and $\sigma_{\text{tot}} = (\sigma_{\text{int}}^2(z) + \sigma_{c,i}^2)^{1/2}$ with $\sigma_{c,i}^2$ being the color error for each individual galaxy.

The calibration of the intercept, $\mathbf{a}(z)$, slope, $\mathbf{s}(z)$, and intrinsic scatter of each color, $\sigma_{\text{int}}(z)$ that constitutes the diagonal element of $\mathbf{C}_{\text{int}}(z)$, follows a sequential approach. Initially, all parameters are estimated with initial guess values. We begin with fitting the intercept first, then update this estimate to refine the slope, and finally adjust the intrinsic scatter. Once all parameters have been individually refined, a final joint calibration is conducted with these updated values serving as the initial guesses. This approach ensures each parameter is optimally tuned, enhancing the overall accuracy and reliability of the red-sequence model. To visualize the calibration results, we present Figure 5, which shows the color-redshift relations for the seed galaxies selected based on a 2000 deg^2 overlap region. The cyan points represent the mean color calibrated at each spline node, while the red short-dashed line indicates the $3\sigma_{\text{int}}$ region. Figure 6 displays the final calibration of all the red-sequence template parameters as a function of redshift for the five colors used in this study. Beyond $z = 1.75$, the spline node parameters of slope and intrinsic scatter for the calibrated template are poorly constrained. This is likely due to the lack of seed galaxies at redshifts $z > 1.75$, as shown in Figure 3 and 5. Additionally, the $z - Y$ color exhibits unusually high intrinsic scatter compared to other colors. This may be due to differences in how photometry is measured in the DC2 catalog and the Roman simulated data, as discussed in Section 2.

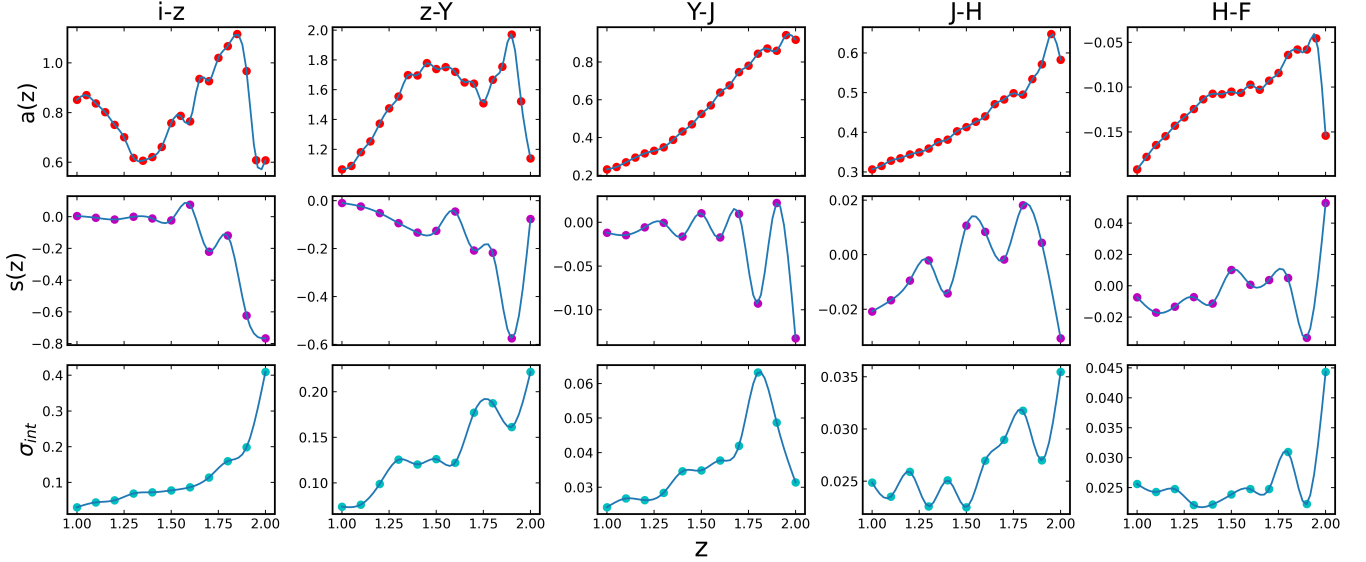


Figure 6. Calibrated Red-sequence parameters as a function of redshift from $z = 1$ to 2. From left to right, each panel displays the trends for different colors: $i - z$, $z - Y$, $Y - J$, $J - H$, and $H - F$. The top panels show the mean color ($C(z)$) across redshift at each redshift node (red points), the middle panels show the slope of the red-sequence template ($S(z)$) at each redshift node (purple points), and the bottom panels show the intrinsic width (σ_{int}) of the fitted color model at each redshift node (cyan points). The solid curves show the fitted spline interpolation function.

3.6. Selection criteria

The selection of LRG candidates in this study applies two criteria following [Rozo et al. \(2016\)](#). The first criterion is a luminosity threshold to ensure that the galaxies are sufficiently luminous. Previous research created two samples based on two luminosity thresholds: a **dense** (hereafter referred to as **highdens**) sample with a luminosity ratio $l > 0.5$ (see Eq. 12), and a **luminous** (hereafter **highlum**) sample with $l > 1$.

The second criterion is a χ^2 cut on the χ^2_{red} (see Equation 7) computed at the best-fit redshift, \widetilde{z}_{red} , which ensures that the selected galaxies closely align with the calibrated red sequence. Previous studies ([Rozo et al. 2016](#); [Vakili et al. 2019](#); [Vakili et al. 2023](#)) implemented a variable $\chi^2(z)$ that adjusts at different redshifts to maintain a constant co-moving density of the samples. In such cases, the derived $\chi^2(z)$ is relatively small (e.g. 2 – 3), resulting in a sample that tightly follows the calibrated red-sequence template. However, it has been noted that while a variable χ^2 cut tends to minimize outliers, it also increases correlations with systematic errors in photometry. Specifically, [Pandey et al. \(2022\)](#) has found that the DES-Y3 RedMaGiC sample derived in this way leads to inconsistencies in the galaxy clustering and galaxy-galaxy lensing results. They proposed that this behavior might be related to unknown systematics that have not been corrected for, such as a color-dependent photometric issue in the DES data. [Pandey et al. \(2022\)](#) further found that this issue can be resolved by loosening the χ^2 threshold via defining a broader, constant $\chi^2 = 8$ cut to the sample. In response to these issues, our study follows [Pandey et al. \(2022\)](#) and applies a simple, constant cut of $\chi^2_{red} \leq 8$ to select LRGs, avoiding the complexities and potential biases introduced by a variable threshold.

3.7. Photo-z afterburner

When the selected IRMaGiC samples having galaxies with spectroscopic information, these galaxies can then be used to calibrate a median redshift offset $\Delta_z(\widetilde{z}_{red}) = z_{spec} - \widetilde{z}_{red}$. And thus obtain the final, refined photometric redshift:

$$z_{red} = \widetilde{z}_{red} + \Delta z(\widetilde{z}_{red}) \quad (22)$$

And $\Delta z(\widetilde{z}_{red})$ parameterized using a spline interpolation, with spline parameters optimized by minimizing the following objective function.:

$$O = \sum_i |z_{spec,i} - \widetilde{z}_{red,i}| \quad (23)$$

To obtain such a sample for afterburner calibration, we applied the *Roman* grism efficiency curves introduced in Section 3.3 to IRMaGiC sample, simulating a scenario in which galaxies with spectroscopic redshifts are available within the sample. The true redshift of selected galaxies are then used for calibration. In this study, we assume that 30% of the galaxies in the highlum/highdens

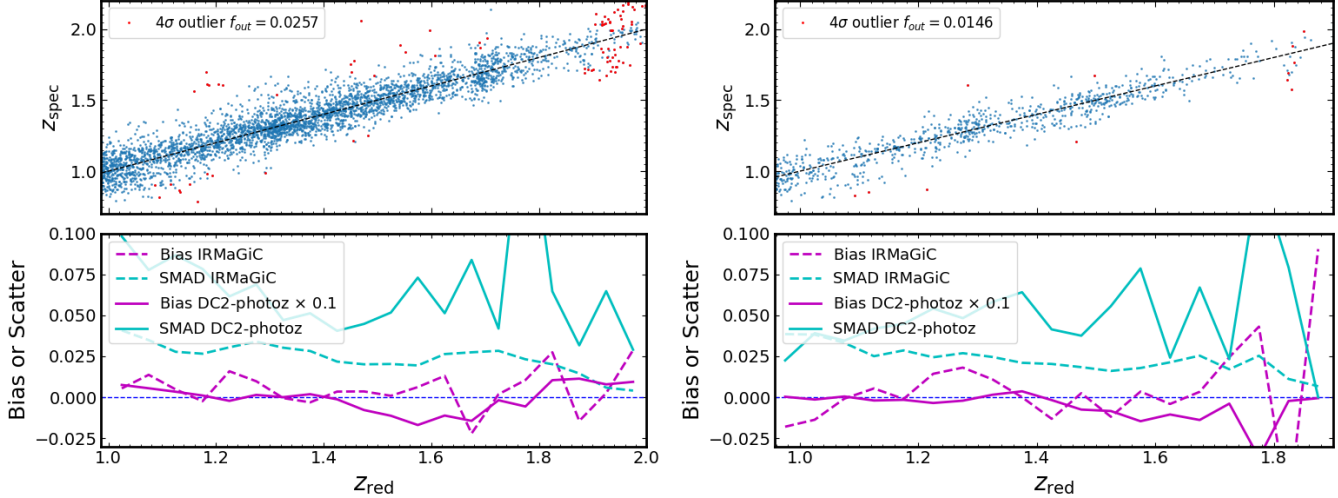


Figure 7. Top panels display the estimated red-sequence photometric redshift z_{red} for galaxies in the **dense**, $L > 0.5L_*$, (left) and **highlum**, $L > L_*$, (right) samples versus their true redshift z_{spec} . The red dots show the 4σ outlier. The bottom panel shows the bias and scatter: the dash (solid) purple line represents the mean bias $z_{\text{red}} - z_{\text{spec}}$ calculated across redshift bins for IRMaGiC redshift (DC2-photoz estimated using BPz), and the cyan dashed (solid) line depicts the scatter or NMAD as defined in Equation 25, across the z_{red} for IRMaGiC redshift (DC2-photoz).

sample will have spectroscopy redshift. Additionally, we can also refine the estimated photometric redshift error, σ_{red} . Assuming the refined error σ_{refine} is given by $\sigma_{\text{refine}} = r(z_{\text{red}})\sigma_{\text{red}}$, and the $r(z_{\text{red}})$ parameter is again characterized by a spline interpolation with best-fit parameters minimizing the objective function:

$$O = \sum_i |1.4826 |z_{\text{red},i} - z_{\text{spec},i}| - r(z_{\text{red},i})\sigma_{\text{red},i}| \quad (24)$$

We refer the reader to [Rozo et al. \(2016\)](#) for more details on this calibration process. After the afterburner step, we recomputed the luminosity ratio l and χ^2_{red} , as discussed in Section 3.6, for every galaxy in the **highdens**/**highlum** sample with refined photometric redshifts and errors.

4. RESULTS

4.1. Photo- z performance

As discussed in Section 3.6, we consider two sets of IRMaGiC sample. The **highdens** sample with galaxies brighter than $0.5L_*$ and the **highlum** sample with galaxies brighter than L_* . Additionally, unless otherwise stated, all the results presented in this section are based on the assumption of a 2000 deg^2 full overlap between LSST and *Roman*. We note that our sample does not have constant comoving density for reasons discussed in Section 3.6. Following [Rozo et al. \(2016\)](#); [Vakili et al. \(2019\)](#), we assess the performance of the IRMaGiC photo- z of the selected galaxies by calculating two quantities in bins of the afterburner calibrated redshift z_{red} . The photometric redshift bias, defined as

the median offset of $\delta_z = z_{\text{spec}} - z_{\text{red}}$, and scatter, defined as Normalised Absolute Median Deviation (NMAD)

$$\text{NMAD} = 1.4826 \times \text{median}(|\Delta_z|) \quad (25)$$

where $\Delta_z = (z_{\text{spec}} - z_{\text{red}})/(1 + z_{\text{spec}})$.

Figure 7 shows the performance of the estimated IRMaGiC photo- z for the **highdens** sample (left-hand panel) and the **highlum** sample (right-hand panel). The purple and cyan dashed lines in the bottom panels present the bias and scatter, binned by z_{red} . Several key points merit attention. First, the **highdens** sample experiences a significant number of 5σ outliers beyond $z_{\text{red}} \approx 1.9$. This can be attributed to the absence of seed galaxies necessary for a well-calibrated red-sequence template in this redshift range as discussed in section 3.5. As indicated in the legend of the top panels, the overall 5σ fraction of the **highdens** sample from $z_{\text{red}} = 1$ to 2 is approximately 4%. However, restricting this to $z_{\text{red}} = 1$ to 1.9, the 5σ outlier rate drops to only 0.09%.

Second, the **highlum** sample contains no galaxies beyond $z_{\text{red}} > 1.8$, which is consistent with the tendency of galaxies to appear fainter at higher redshifts and the luminosity threshold of the **highlum** sample, which targets exceptionally bright galaxies. We report the mean bias and scatter for the **highdens** and **highlum** samples as $(3.2 \times 10^{-3}, 0.026)$ and $(3.3 \times 10^{-3}, 0.022)$, calculated within the redshift ranges of $z_{\text{red}} = 1 - 1.9$ and $z_{\text{red}} = 1 - 1.8$ respectively. Focusing on the scatter within the **highdens** sample, we observe that the three highest scatter values occur at $z_{\text{red}} \approx 1, 1.3$, and 1.8, re-

spectively. This pattern can be explained by the transition of the 4000Å break across different filters: it moves from the LSST i-band to the LSST z-band at $z \approx 1$, from the LSST z-band to the Roman F106 band at $z \approx 1.3$, and from the Roman F106 band to the Roman F129 band at $z \approx 1.8$ as illustrated in Figure 1.

4.2. Comparing with DC2 photo- z

We now evaluate the performance of IRMaGiC photo- z alongside other photo- z algorithms within the DC2 catalog, which we term as DC2-photo z in this paper, for each galaxy. These estimates are derived from the Bayesian Photometric Redshift (BPz) code, which leverages Bayesian probability to enhance redshift estimate accuracy. This method incorporates prior probabilities and applies Bayesian marginalization, integrating critical data such as redshift distributions and galaxy type mixes into the estimation process, thus enhancing precision. We refer readers to [Benítez \(2000\)](#); [Schmidt et al. \(2020\)](#) for further details. Notably, the LSST-DESC Redshift Assessment Infrastructure Layer (RAIL) ([Schmidt et al. 2023](#)), a framework for photometric redshift estimation and analysis for LSST-DESC, implements a similar version of the BPz code. Therefore, the recorded photo- z values provide an excellent preview of the quality of LSST photo- z s. In the bottom panels of Figure 7, we show the bias (purple, solid line) and scatter (cyan, solid line) of DC2-photo z s for the `highdens` and `highlum` samples. Note that we scale the bias of DC2-photo z s down by a factor of 10 for easier comparison with the IRMaGiC photo- z performance. The mean bias and scatter of the DC2-photo z are (-0.016, 0.069) and (-0.057, 0.05) for the `highdens` and `highlum` samples respectively. Comparing values of IRMaGiC photo- z in Section 4.1, it is clear that IRMaGiC photo- z s outperform DC2-photo z . This suggests that the inclusion of additional data from the Roman Space Telescope could further refine the photometric redshift estimates of LSST galaxies beyond those achievable using LSST data alone.

4.3. Comparing with low- z LRG samples

The original RedMaPPer and RedMaGiC algorithms have been applied to LSST cosmoDC2/DC2 galaxies using only LSST photometry to generate LRG samples in the redshift range of $0 < z < 1$. The cosmoDC2/DC2 RedMaGiC sample applies constant χ^2 cut for LRG selection, rather than a variable χ^2 , for the same reasons discussed in Section 3.6. In this section, we compare our IRMaGiC samples to the LSST DC2 RedMaGiC samples. Figure 8 illustrates the redshift performance comparison for the `highdens`/`highlum` samples from the

LSST DC2 and IRMaGiC. As mentioned in Section 4.1, our LRG samples exhibit greater scatter compared to other low- z RedMaGiC or RedMaGiC-like samples, this is also clearly shown in the bottom panel of Figure 8.

This increased scatter could be due to three factors. First, the underlying truth magnitudes for each galaxy differ between cosmoDC2, which the DC2 simulation is based on, and the Roman truth catalog. In cosmoDC2, the `mag_norm` values used to scale the input galaxy SEDs vary across different bandpasses ([LSST Dark Energy Science Collaboration \(LSST DESC\) et al. 2021](#)), while the Roman simulation uses a constant `mag_norm` to scale the SEDs across all Roman bands ([Troxel et al. 2023](#)). This difference in truth magnitude calculation may contribute to the increased scatter. Second, as noted in Section 2, the photometry in the two catalogs is measured differently, which could also contribute to the increased scatter. Third, red and blue galaxy populations tend to be blended more at higher redshifts, which broadens the intrinsic scatter of the red sequence template.

To explore this further, we rerun the IRMaGiC algorithm on the truth catalog for the LSST-Roman joint galaxy sample. We calibrate a red-sequence model based on ground-truth information and compare the redshift performance to the cosmoDC2 RedMaGiC samples. Comparing results derived based on galaxy truth photometry allows us to rule out the impact of measured photometry. Our comparison shows that, despite differing assumptions about the scaling of galaxy SEDs and our sample being at higher redshifts, the scatters are comparable in this case. Further details can be found in Appendix A. Thus, we conclude that the observed increase in scatter is likely due to the lack of calibration of the Roman photometry.

Moreover, Figure 8 demonstrates the significant extension of existing LRG samples to higher redshifts by combining data from LSST and *Roman*. Expanding the LRG sample at higher redshifts is crucial for improving future cosmological analyses. For example, in the HSC Y3 weak lensing study, the tomographic redshift distribution was inferred by combining individual photo- z posteriors with cross-correlation measurements of the HSC CAMIRA LRG sample. However, the redshift distribution could not be fully calibrated due to the absence of a reliable calibration sample of CAMIRA LRGs at $z \geq 1$ ([Rau et al. 2023](#); [Miyatake et al. 2023](#)). The extended LRG sample from LSST and *Roman* will help resolve similar issues in the future, enabling more accurate redshift calibration at higher redshifts and ultimately leading to tighter cosmological constraints.

4.4. Redshift coverage as a function of overlapping area

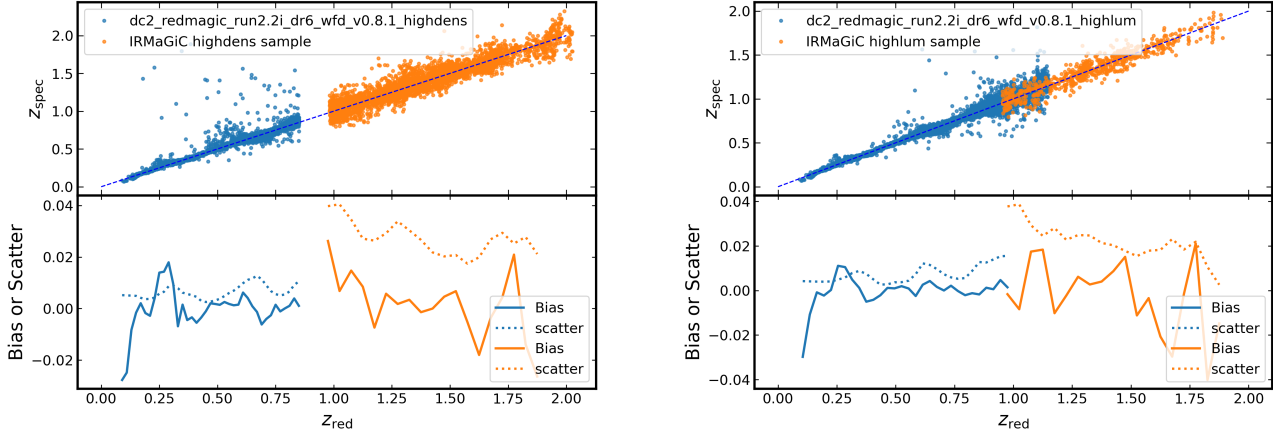


Figure 8. Combination of the DC2 RedMaGiC sample and LRG samples presented in this study. The left plot shows the combined highdens sample, the right plot shows the combined highlum sample. Top panels show the estimated redshift from the two samples versus true redshift z_{spec} . The bottom panels show the bias (solid line) and Scatter/NMAD (dotted line) of the two samples.

Table 1. Photometric redshift performance of the highdens and highlum IRMaGiC galaxy samples for different overlapping areas between LSST and *Roman*. z_{max} is the maximum redshift range of the sample.

Overlapping area (deg ²)	Highdens				Highlum			
	z_{max}	Bias (%)	Scatter (%)	Outlier (%)	z_{max}	Bias (%)	Scatter (%)	Outlier (%)
20	1.7	0.21	3.05	1.30	1.68	0.7	2.48	1.41
40	1.72	0.31	2.60	1.70	1.72	0.5	2.5	0.71
100	1.82	0.36	2.56	1.07	1.76	0.75	2.39	1.53
200	1.88	0.13	2.70	1.36	1.8	0.39	2.36	0.43
500	1.92	0.26	2.64	1.68	1.79	0.79	2.33	1.16
1000	1.92	0.15	2.65	1.06	1.8	0.16	2.4	0.57
2000	1.93	0.14	2.63	1.01	1.81	0.04	2.3	1.2

The analysis thus far has assumed a complete overlap of 2000 deg² between the LSST and the *Roman* surveys. In this section, we expand our examination to assess the impact of varying the size of the overlap region on our results. Following the methodology outlined in Section 3.4, in addition to the initial 2000 deg² template, we calibrated additional red-sequence templates for overlap regions of 20 deg², 40 deg², 100 deg², 500 deg², and 1000 deg². For each newly calibrated template, we run on the same galaxy sample to calculate the mean bias, mean scatter, outlier rate, and to determine the maximum redshift coverage. The final maximum redshift for each scenario is determined based on visual inspections, where a significant rise in the frequency of 5 σ outliers indicates the limit of reliable redshift. The com-

prehensive results of these analyses are summarized in Table 1, detailing the effects of each overlap scenario on IRMaGiC photo-z performance. The most substantial improvements in redshift coverage occur from 40 deg² ($z_{\text{max}} = 1.72/1.72$) to 100 deg² ($z_{\text{max}} = 1.82/1.76$) and from 100 deg² to 200 deg² ($z_{\text{max}} = 1.88/1.8$). Beyond a 500 deg² overlap, further improvements in redshift coverage are minimal. Therefore, an overlap region of at least 200 deg² is necessary for IRMaGiC to achieve reliable redshift measurements up to $z \approx 1.9$ and 1.8 for each sample respectively.

5. SUMMARY

In this paper, we develop a RedMaGiC-like algorithm to identify luminous red galaxies (LRGs) in the redshift range of $1 \leq z \leq 2$ using simulated data from two Stage IV dark energy surveys: the Vera C. Rubin Observa-

tory’s Legacy Survey of Space and Time (LSST) and the Nancy Grace Roman Space Telescope’s High Latitude Wide-Area Survey. We utilize the complementary wavelength coverage of LSST’s optical bands and Roman HLIS’s infrared bands to extend the red-sequence calibration to higher redshifts.

Our method involves cross-matching simulated photometric data from LSST and Roman HLIS and using the Roman High Latitude Spectroscopy Survey (HLSS) to supply spectroscopically confirmed red galaxies for the red-sequence template calibration. We present a new strategy for selecting high-redshift red galaxy candidates and calibrating the red-sequence template, which allows for accurate photometric redshift estimates. The performance of our algorithm is evaluated using two luminosity thresholds for LRG selection.

The results show that our RedMaGiC-like algorithm achieves robust photometric redshift accuracy, outperforming existing photometric redshift estimation methods in the LSST DC2 catalog. Additionally, we explore the impact of the overlap region size between LSST and Roman on redshift coverage and find that an overlap of at least 200 deg^2 is necessary to reliably extend redshift measurements to $z \approx 1.9$. These findings highlight the potential of joint LSST-Roman observations to enhance LRG selection and photometric redshift estimation for cosmological studies.

¹ This paper has undergone internal review by the LSST
² Dark Energy Science Collaboration. The internal re-
³ viewers were Irene Moskowitz and Anna Porredon.

⁴ ZG and CW were supported by Department of Energy,
⁵ grant DE-SC0010007.

⁶ The DESC acknowledges ongoing support from the
⁷ Institut National de Physique Nucléaire et de Physique
⁸ des Particules in France; the Science & Technology Fa-
⁹ cilities Council in the United Kingdom; and the Depart-
¹⁰ ment of Energy, the National Science Foundation, and
¹¹ the LSST Corporation in the United States. DESC uses
¹² resources of the IN2P3 Computing Center (CC-IN2P3-
¹³ Lyon/Villeurbanne - France) funded by the Centre Na-
¹⁴ tional de la Recherche Scientifique; the National Energy
¹⁵ Research Scientific Computing Center, a DOE Office of
¹⁶ Science User Facility supported by the Office of Science
¹⁷ of the U.S. Department of Energy under Contract No.
¹⁸ DE-AC02-05CH11231; STFC DiRAC HPC Facilities,
¹⁹ funded by UK BEIS National E-infrastructure capital
²⁰ grants; and the UK particle physics grid, supported by
²¹ the GridPP Collaboration. This work was performed in
²² part under DOE Contract DE-AC02-76SF00515.

²³ The contributions from the primary authors are as
²⁴ follows. ZG analysed data, and wrote the paper. CW
²⁵ supervised the project and analysis. E.R. contributed
²⁶ expertise and code related to the Red-Sequence fitting
²⁷ algorithm used in RedMapper and RedMaGiC.

APPENDIX

A. IRMAGIC PHOTOMETRIC REDSHIFT PERFORMANCE ON TRUTH CATALOGS

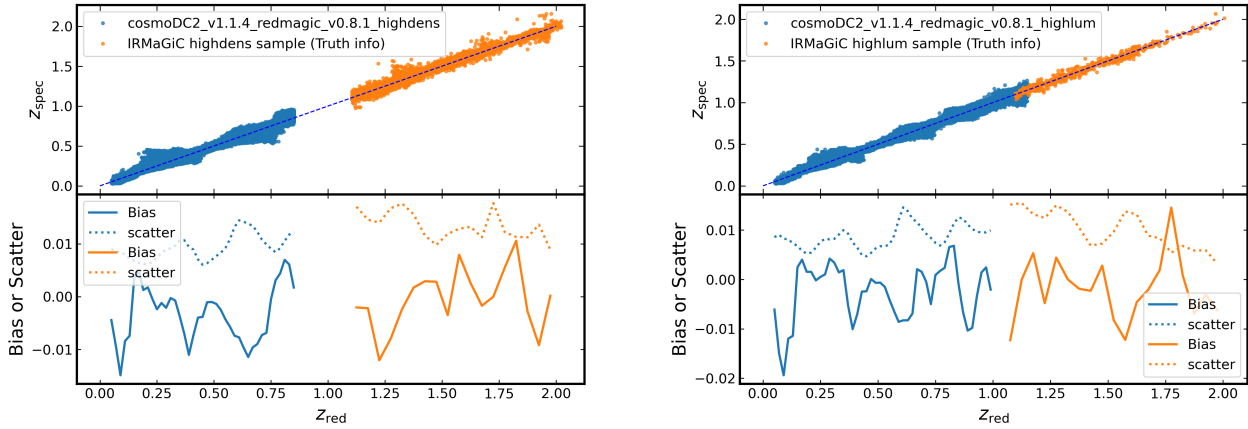


Figure 9. Photometric redshift performance comparison of the cosmoDC2 RedMaGiC samples and LRG samples derived based on truth catalog in this study for the highdens and highlum samples relatively. Top panels shows z_{red} versus z_{spec} . The bottom panels shows bias (solid line) the NMAD (dotted line).

In Section 3.5, we reported unusually high intrinsic scatter across the spline nodes for the $z - Y$ color. Moreover, in Section 4.2, the LRG catalog generated in this study exhibited greater scatter than that of the low-redshift DC2 RedMaGiC catalog. This discrepancy might be attributed to the photometric measurements in the Roman galaxy sample. To further explore this issue, we utilized the galaxy truth photometry (specifically, i and z magnitude for LSST and Y, J, H, F magnitude for Roman) from input truth catalogs to calibrate a red-sequence model based on ground-truth information and compare the calibration results and RedMaGiC redshift performance. For the Roman data, the truth catalog provided by Troxel et al. (2023), for the LSST data, we cross-match the galaxy id from the Roman truth catalog with the cosmoDC2 catalog, `cosmoDC2_v1.1.4_image`. The original RedMaGiC algorithm was applied to the cosmoDC2 sample to generate LRG samples, `cosmoDC2_v1.1.4_redmagic_v0.8.1_highdens` and `cosmoDC2_v1.1.4_redmagic_v0.8.1_highlum`, using LSST-only truth photometry (g,r,i,z,y) in the redshift range of $0 < z < 1$. We compare our results with the cosmoDC2 LRG samples in Figure 9 and the bottom panel displays the scatter as a function of z_{red} . For comparison of both the highdens and highlum samples, the scatter in the high-redshift LRG samples from this study is comparable to that in the low-redshift cosmoDC2 LRG samples. This suggests that the observed increased scatter in high-redshift LRG samples is not due to deficiencies in the RedMaGiC algorithm but rather calibration issues with the photometry of the Roman simulated galaxy sample.

REFERENCES

- Aihara, H., Arimoto, N., Armstrong, R., et al. 2018, PASJ, 70, S4, doi: [10.1093/pasj/pss066](https://doi.org/10.1093/pasj/pss066)
- Akeson, R., Armus, L., Bachelet, E., et al. 2019, arXiv e-prints, arXiv:1902.05569, doi: [10.48550/arXiv.1902.05569](https://doi.org/10.48550/arXiv.1902.05569)
- Albrecht, A., Bernstein, G., Cahn, R., et al. 2006, arXiv e-prints, astro, doi: [10.48550/arXiv.astro-ph/0609591](https://doi.org/10.48550/arXiv.astro-ph/0609591)
- Benítez, N. 2000, ApJ, 536, 571, doi: [10.1086/308947](https://doi.org/10.1086/308947)
- Bertin, E., & Arnouts, S. 1996, A&AS, 117, 393, doi: [10.1051/aas:1996164](https://doi.org/10.1051/aas:1996164)
- Beverage, A. G., Slob, M., Kriek, M., et al. 2024, arXiv e-prints, arXiv:2407.02556, doi: [10.48550/arXiv.2407.02556](https://doi.org/10.48550/arXiv.2407.02556)
- Bisigello, L., Kuchner, U., Conselice, C. J., et al. 2020, MNRAS, 494, 2337, doi: [10.1093/mnras/staa885](https://doi.org/10.1093/mnras/staa885)
- Brammer, G. 2019, Grizli: Grism redshift and line analysis software, Astrophysics Source Code Library, record ascl:1905.001
- Bruzual, G., & Charlot, S. 2003, MNRAS, 344, 1000, doi: [10.1046/j.1365-8711.2003.06897.x](https://doi.org/10.1046/j.1365-8711.2003.06897.x)
- Carnero Rosell, A., Rodriguez-Monroy, M., Crocce, M., et al. 2022, MNRAS, 509, 778, doi: [10.1093/mnras/stab2995](https://doi.org/10.1093/mnras/stab2995)
- Choi, J., Conroy, C., Moustakas, J., et al. 2014, ApJ, 792, 95, doi: [10.1088/0004-637X/792/2/95](https://doi.org/10.1088/0004-637X/792/2/95)
- Crocce, M., Ross, A. J., Sevilla-Noarbe, I., et al. 2019, MNRAS, 482, 2807, doi: [10.1093/mnras/sty2522](https://doi.org/10.1093/mnras/sty2522)
- Dark Energy Survey Collaboration, Abbott, T., Abdalla, F. B., et al. 2016, MNRAS, 460, 1270, doi: [10.1093/mnras/stw641](https://doi.org/10.1093/mnras/stw641)
- de Jong, J. T. A., Verdoes Kleijn, G. A., Kuijken, K. H., & Valentijn, E. A. 2013, Experimental Astronomy, 35, 25, doi: [10.1007/s10686-012-9306-1](https://doi.org/10.1007/s10686-012-9306-1)
- de Jong, J. T. A., Verdoes Kleijn, G. A., Erben, T., et al. 2017, A&A, 604, A134, doi: [10.1051/0004-6361/201730747](https://doi.org/10.1051/0004-6361/201730747)
- DESI Collaboration, Adame, A. G., Aguilar, J., et al. 2024, arXiv e-prints, arXiv:2404.03000, doi: [10.48550/arXiv.2404.03000](https://doi.org/10.48550/arXiv.2404.03000)
- Driver, S. P., Hill, D. T., Kelvin, L. S., et al. 2011, Monthly Notices of the Royal Astronomical Society, 413, 971, doi: [10.1111/j.1365-2966.2010.18188.x](https://doi.org/10.1111/j.1365-2966.2010.18188.x)
- Edge, A., Sutherland, W., Kuijken, K., et al. 2013, The Messenger, 154, 32
- Eifler, T., Miyatake, H., Krause, E., et al. 2021, Monthly Notices of the Royal Astronomical Society, 507, 1746, doi: [10.1093/mnras/stab1762](https://doi.org/10.1093/mnras/stab1762)
- Eisenstein, D. J., Annis, J., Gunn, J. E., et al. 2001, AJ, 122, 2267, doi: [10.1086/323717](https://doi.org/10.1086/323717)
- Florez, J., Jogee, S., Sherman, S., et al. 2020, MNRAS, 497, 3273, doi: [10.1093/mnras/staa2200](https://doi.org/10.1093/mnras/staa2200)
- Fontanot, F., De Lucia, G., Monaco, P., Somerville, R. S., & Santini, P. 2009, MNRAS, 397, 1776, doi: [10.1111/j.1365-2966.2009.15058.x](https://doi.org/10.1111/j.1365-2966.2009.15058.x)
- Guo, Z., Joshi, B., Walter, C. W., & Troxel, M. A. 2024, arXiv e-prints, arXiv:2411.08035, doi: [10.48550/arXiv.2411.08035](https://doi.org/10.48550/arXiv.2411.08035)
- Heitmann, K., Finkel, H., Pope, A., et al. 2019, ApJS, 245, 16, doi: [10.3847/1538-4365/ab4da1](https://doi.org/10.3847/1538-4365/ab4da1)
- Ivezic, Ž., Kahn, S. M., Tyson, J. A., et al. 2019, ApJ, 873, 111, doi: [10.3847/1538-4357/ab042c](https://doi.org/10.3847/1538-4357/ab042c)
- Khullar, G., Bayliss, M. B., Gladders, M. D., et al. 2022, ApJ, 934, 177, doi: [10.3847/1538-4357/ac7c0c](https://doi.org/10.3847/1538-4357/ac7c0c)
- Korytov, D., Hearin, A., Kovacs, E., et al. 2019, ApJS, 245, 26, doi: [10.3847/1538-4365/ab510c](https://doi.org/10.3847/1538-4365/ab510c)
- LSST Dark Energy Science Collaboration. 2012, arXiv e-prints, arXiv:1211.0310, doi: [10.48550/arXiv.1211.0310](https://doi.org/10.48550/arXiv.1211.0310)
- LSST Dark Energy Science Collaboration, Abolfathi, B., Armstrong, R., et al. 2021, arXiv e-prints, arXiv:2101.04855, doi: [10.48550/arXiv.2101.04855](https://doi.org/10.48550/arXiv.2101.04855)
- LSST Dark Energy Science Collaboration (LSST DESC), Abolfathi, B., Alonso, D., et al. 2021, ApJS, 253, 31, doi: [10.3847/1538-4365/abd62c](https://doi.org/10.3847/1538-4365/abd62c)
- LSST Science Collaboration, Abell, P. A., Allison, J., et al. 2009, arXiv e-prints, arXiv:0912.0201, doi: [10.48550/arXiv.0912.0201](https://doi.org/10.48550/arXiv.0912.0201)
- Marsan, Z. C., Muzzin, A., Marchesini, D., et al. 2022, ApJ, 924, 25, doi: [10.3847/1538-4357/ac312a](https://doi.org/10.3847/1538-4357/ac312a)
- Miyatake, H., Sugiyama, S., Takada, M., et al. 2023, PhRvD, 108, 123517, doi: [10.1103/PhysRevD.108.123517](https://doi.org/10.1103/PhysRevD.108.123517)
- Oguri, M. 2014, MNRAS, 444, 147, doi: [10.1093/mnras/stu1446](https://doi.org/10.1093/mnras/stu1446)
- Oguri, M., Lin, Y.-T., Lin, S.-C., et al. 2017a, Publications of the Astronomical Society of Japan, 70, S20, doi: [10.1093/pasj/psx042](https://doi.org/10.1093/pasj/psx042)
- . 2017b, Publications of the Astronomical Society of Japan, 70, S20, doi: [10.1093/pasj/psx042](https://doi.org/10.1093/pasj/psx042)
- Padmanabhan, N., Schlegel, D. J., Seljak, U., et al. 2007, MNRAS, 378, 852, doi: [10.1111/j.1365-2966.2007.11593.x](https://doi.org/10.1111/j.1365-2966.2007.11593.x)
- Pandey, S., Krause, E., DeRose, J., et al. 2022, PhRvD, 106, 043520, doi: [10.1103/PhysRevD.106.043520](https://doi.org/10.1103/PhysRevD.106.043520)
- Paspaliaris, E. D., Xilouris, E. M., Nersesian, A., et al. 2023, A&A, 669, A11, doi: [10.1051/0004-6361/202244796](https://doi.org/10.1051/0004-6361/202244796)
- Pedregosa, F., Varoquaux, G., Gramfort, A., et al. 2011, Journal of Machine Learning Research, 12, 2825
- Percival, W. J., Cole, S., Eisenstein, D. J., et al. 2007, MNRAS, 381, 1053, doi: [10.1111/j.1365-2966.2007.12268.x](https://doi.org/10.1111/j.1365-2966.2007.12268.x)

- Rau, M. M., Dalal, R., Zhang, T., et al. 2023, MNRAS, 524, 5109, doi: [10.1093/mnras/stad1962](https://doi.org/10.1093/mnras/stad1962)
- Rozo, E., Rykoff, E. S., Abate, A., et al. 2016, MNRAS, 461, 1431, doi: [10.1093/mnras/stw1281](https://doi.org/10.1093/mnras/stw1281)
- Rykoff, E. S., Rozo, E., Busha, M. T., et al. 2014, ApJ, 785, 104, doi: [10.1088/0004-637X/785/2/104](https://doi.org/10.1088/0004-637X/785/2/104)
- Rykoff, E. S., Rozo, E., Hollowood, D., et al. 2016, ApJS, 224, 1, doi: [10.3847/0067-0049/224/1/1](https://doi.org/10.3847/0067-0049/224/1/1)
- Sailer, N., Kim, J., Ferraro, S., et al. 2024, arXiv e-prints, arXiv:2407.04607, doi: [10.48550/arXiv.2407.04607](https://doi.org/10.48550/arXiv.2407.04607)
- Salpeter, E. E. 1955, ApJ, 121, 161, doi: [10.1086/145971](https://doi.org/10.1086/145971)
- Schmidt, S., Gschwend, J., Crenshaw, J. F., et al. 2023, LSSTDESC/RAIL: v0.98.5, v0.98.5, Zenodo, doi: [10.5281/zenodo.7927358](https://doi.org/10.5281/zenodo.7927358)
- Schmidt, S. J., Malz, A. I., Soo, J. Y. H., et al. 2020, MNRAS, 499, 1587, doi: [10.1093/mnras/staa2799](https://doi.org/10.1093/mnras/staa2799)
- Slob, M., Kriek, M., Beverage, A. G., et al. 2024, arXiv e-prints, arXiv:2404.12432, doi: [10.48550/arXiv.2404.12432](https://doi.org/10.48550/arXiv.2404.12432)
- Spergel, D., Gehrels, N., Baltay, C., et al. 2015, arXiv e-prints, arXiv:1503.03757, doi: [10.48550/arXiv.1503.03757](https://doi.org/10.48550/arXiv.1503.03757)
- Stefanon, M., Marchesini, D., Rudnick, G. H., Brammer, G. B., & Whitaker, K. E. 2013, ApJ, 768, 92, doi: [10.1088/0004-637X/768/1/92](https://doi.org/10.1088/0004-637X/768/1/92)
- The LSST Dark Energy Science Collaboration, Mandelbaum, R., Eifler, T., et al. 2018, arXiv e-prints, arXiv:1809.01669, doi: [10.48550/arXiv.1809.01669](https://doi.org/10.48550/arXiv.1809.01669)
- Troxel, M. A., Lin, C., Park, A., et al. 2023, MNRAS, 522, 2801, doi: [10.1093/mnras/stad664](https://doi.org/10.1093/mnras/stad664)
- Vakili, M., Bilicki, M., Hoekstra, H., et al. 2019, Monthly Notices of the Royal Astronomical Society, 487, 3715, doi: [10.1093/mnras/stz1249](https://doi.org/10.1093/mnras/stz1249)
- Vakili, M., Hoekstra, H., Bilicki, M., et al. 2023, A&A, 675, A202, doi: [10.1051/0004-6361/202039293](https://doi.org/10.1051/0004-6361/202039293)
- Visvanathan, N., & Sandage, A. 1977, ApJ, 216, 214, doi: [10.1086/155464](https://doi.org/10.1086/155464)
- Wang, Y., Zhai, Z., Alavi, A., et al. 2022, ApJ, 928, 1, doi: [10.3847/1538-4357/ac4973](https://doi.org/10.3847/1538-4357/ac4973)
- White, M., Zhou, R., DeRose, J., et al. 2022, JCAP, 2022, 007, doi: [10.1088/1475-7516/2022/02/007](https://doi.org/10.1088/1475-7516/2022/02/007)
- Yuan, S., Blake, C., Krolewski, A., et al. 2024, MNRAS, 533, 589, doi: [10.1093/mnras/stae1792](https://doi.org/10.1093/mnras/stae1792)
- Zhou, R., Dey, B., Newman, J. A., et al. 2023a, AJ, 165, 58, doi: [10.3847/1538-3881/aca5fb](https://doi.org/10.3847/1538-3881/aca5fb)
- Zhou, R., Ferraro, S., White, M., et al. 2023b, JCAP, 2023, 097, doi: [10.1088/1475-7516/2023/11/097](https://doi.org/10.1088/1475-7516/2023/11/097)
- Zhou, R., Dey, B., Newman, J. A., et al. 2023c, AJ, 165, 58, doi: [10.3847/1538-3881/aca5fb](https://doi.org/10.3847/1538-3881/aca5fb)
- Zhuang, Z., Leethochawalit, N., Kirby, E. N., et al. 2023, ApJ, 948, 132, doi: [10.3847/1538-4357/acc79b](https://doi.org/10.3847/1538-4357/acc79b)